Fractal fragmentation of rocks within sturzstroms: insight derived from physical experiments within the ETH geotechnical drum centrifuge

Bernd Imre · Jan Laue · Sarah Marcella Springman

Abstract An investigation of the behaviour and energy budget of sturzstroms has been carried out using physical, analytical and numerical modelling techniques. Sturzstroms are rock slides of very large volume and extreme run out, which display intensive fragmentation of blocks of rock due to inter-particle collisions within a collisional flow. Results from centrifugal model experiments provide strong arguments to allow the micro-mechanics and energy budget of sturzstroms to be described quantitatively by a fractal comminution model. A numerical experiment using a distinct element method (DEM) indicates rock mass and boundary conditions, which allow an alternating fragmenting and dilating dispersive regime to evolve and to sustain for long enough to replicate the spreading and run out of sturzstroms without needing to resort to peculiar mechanism. The fragmenting spreading model supported here is able to explain the run out of a fluid-absent granular flow beyond the travel distance predicted by a Coulomb frictional sliding model. This, and its strong relation to internal fragmentation, suggests that a sturzstrom constitutes a landslide category of its own. This study provides a novel framework for the understanding the physics of such sturzstroms.

Keywords Centrifuge modelling · Distinct element modelling · Fractal fragmentation · Rock avalanche · Rock mechanics · Sturzstrom

B. Imre (✉) · J. Laue · S. M. Springman
Institute for Geotechnical Engineering, ETH Zurich,
8093 Zurich, Switzerland
e-mail: bernd.imre@igt.baug.ethz.ch

1 Introduction

The downslope mass movement of dry, loose rock material is a common geological process. Such events are often referred to as dry rock falls, rock slides or rock topple [1]. The mechanics of such phenomena are generally well understood in terms of the competition between gravity, inertia and inter-granular friction (e.g. [2–5] and others). However, a rare category of dry rock slides, or in few cases rock falls, exists in which vast horizontal distances are travelled with only a comparatively small vertical drop in height. They turn into sturzstroms (Fig. 1; [6]) during run out and appear to travel as if the inter-granular coefficient of friction, which usually controls the downslope motion of dry rock debris, is temporarily reduced by an order of magnitude or more ([7–9] and others). Confronted with this evidence, the Swiss geologist Albert Heim asked: "Wie kann dieses Blockwerk sich auf diesem ebenen Talboden so ausgebreitet haben? Wasser, Schlamm-Muhrgänge könnten das nicht tun; und das Blockwerk ist trocken und war trocken!" ("How can a blocky rock mass spread itself in such a way? Debris flows could not do it; and the rock mass was dry and is dry!" [10]). In our opinion, this question still remains largely unresolved today.

The present study is part of a research effort to investigate sturzstroms numerically by distinct element modelling [11–14] and physically within the ETH geotechnical drum centrifuge [15]. Both modelling methods adopt highly specialized tools, which allow fundamental research to be performed. A more rigorous language is therefore necessary to describe the epistemological implications (among others [16–18]), which goes beyond the usual needs and requirements of civil engineering [19,20].

In the theory of epistemology, single localizable and datable events are referred to as "tokens". General and repetitive

Fig. 1 Contemporary painting of the Goldau sturzstrom of 1806 modified after W. U. Oppermann (1810), seen from the Mt. Rigi Kulm. The outline of the deposit is indicated by a *dotted line*. (S1) denotes the centre of mass of the source at an altitude of ∼1300 m a.s.l and (S2) the ∼centre of mass at about 500 m a.s.l. The horizontal distance between S1 and S2 amounts about to 3500 m [51]. (G) indicates the former position of Goldau village (∼510 m a.s.l.), which was annihilated completely by the sturzstrom together with several other hamlets. (*LL*) indicates Lake Lauerz (447 m a.s.l.). The positive $x'(t)$-axis points in the direction parallel to the main flow of the sturzstrom, to define the sign convention. It defines a moving coordinate system whose origin is depended on time t. In perpendicular directions, the $y'(t)$-axis defines the horizontal width of the flow, and the $z'(t)$-axis its thickness

processes and features, referred to as "types" may be induced from these tokens (e.g. [16]). Based on literature review and own observations, three types can be identified which, seem to be common to all known cases of sturzstroms [21]: (1) Run out increases significantly with failure volume [7,22–25]. (2) Sturzstrom deposits are intensively fragmented (Figs. 2, 3; among others [10,21,26–37]). (3) The initial stratigraphy of the source is preserved in the deposits, suggesting little turbulence within the flow [6,10,38].

Current scientific explanations are imaginative, variable and fail to account for all of the universal type-features presented above (for a review on mechanisms proposed, see among others [24,36,39–43]). It is obvious that a sturzstrom represents a highly dynamic collisional granular regime [7,44,45]. Thus particles do not only collide but will eventually crush each other. Erismann and Abele [36] describe this process as dynamic disintegration, where kinetic energy is the main driver for fragmenting the rock mass. The comparatively new fragmentation-spreading model identifies fragmentation as a key parameter for the long run out of sturzstroms [23,46–50]. The aim of the present study is to increase the understanding of the role of rock fragmentation within such highly mobile rock masses.

2 Physical experiments

2.1 Field evidence

The Goldau sturzstrom that occurred in 1806 (canton Schwyz/Switzerland; [10,51–56]) is a single sturzstrom event or, from the epistemological view point, a token (Fig. 1). It displays all type-features of sturzstroms as mentioned above, paired with a very simple geometry, and an excellent availability of data and first hand eyewitness accounts. This sturzstrom was therefore selected to serve as prototype for the present research project (in civil engineering, a "prototype" is an idealized representation of an object of study and its type-features; e.g. [20]). Data of the fabric, particle size distributions and particle shapes have been collected for this study from this site. Further samples have been collected from the deposits of sturzstroms in Flims (canton Graubünden/Switzerland; [31,32,54,57–60]), Grächen (canton Valais/Switzerland; [9,61]) and Köfels (Tyrol/Austria; [54,62–64]). The deposits sampled from all these sites are characterized by a fairly uniform matrix supported fabric. Despite intense fragmentation, large rock boulders can be found at any depth (Fig. 3). All sampled particles,

Fig. 2 Present day view on the detachment zone of the Goldau sturzstrom of 1806 *at the top* of Mt. Rossberg (1558 m a.s.l.). The *large blocks* of conglomerate, bounded by widely spaced joints, are clearly visible (a person serves as scale)

Fig. 3 Present day view on a road-cut through the upper few metres of the deposit of the Goldau sturzstrom of 1806, close to the zoological garden in Goldau (514 m a.s.l.). The quasi-matrix supported fabric of the highly fragmented conglomerate is clearly visible. Note the accumulation of *large blocks on top* (the 5 m long tube in front serves as scale)

Fig. 4 Chunks of massive, micritic Malm limestone sampled from the sturzstrom of Flims. This sample is representative of the angularity of particles forming in sturzstroms—independent from their diameter and geology. The rough fracture surfaces are not pre-existent in the source rock but are newly formed by fragmentation during the transition of the sturzstrom. These two chunks fit together like a "jigsaw puzzle" [114,115]. The *white spots* are lunette shaped impact marks by other rocks, but no signs of abrasion are observable (a 27 mm dia. coin serves as scale)

at any size, display sharp edges with angular shape, while virtually no signs of abrasion can be found. Instead white, lunette shaped impact marks appear regularly, which are most visible on the micritic Malm limestone of the Flims sturzstrom (Fig. 4). These features are not new. Heim [10] described them quite accurately already, but the resulting implications on the thermodynamics of sturzstroms have not been fully elaborated since then.

2.2 Centrifuge modelling of fragmentation

Fundamental research on the failure of rock (among others [65–71]) reveals that fragmentation constitutes a path of energy dissipation. Because sturzstroms are accompanied by intensive particle fragmentation (Sect. 1), it is therefore necessary to consider it for the understanding of the thermodynamics of sturzstroms. Unfortunately, fragmentation within sturzstroms can not be observed directly in a real event because of their long "reoccurrence time" and the obvious difficulties in placing measuring devices within such a rock flow.

Physical experiments on rock slides have been performed within the ETH Geotechnical Drum Centrifuge [15] to enable significantly higher kinetic energies and stresses levels, much closer to the prototype situation, to be applied to rock material, in contrast with so-called 1*g* (gravity) laboratory experiments. The intention of these experiments is to make fragmentation within sturzstroms observable and reproducible. Hence, they have been performed to provide empirical data on which a hypothesis on the run out of sturzstroms may be induced. These experiments are not intended to test, or to deduce predictions on the run out of true sturzstroms; for the difference between induction and deduction (see e.g. [16]).

The physical model in the geotechnical centrifuge simulates an environment of a virtual unconfined run out in the direction of the local x'-axis, plane strain conditions in the local y'-axis, a free surface in the positive z'-direction and a smooth, hard sliding surface in the negative z'-axis of the sliding mass (Fig. 5a). This basic set up is inspired by the direction of the stresses of sturzstroms in nature. The thickness of a sturzstrom is small compared to its lateral and longitudinal extensions. The propositions are made that the largest nor-
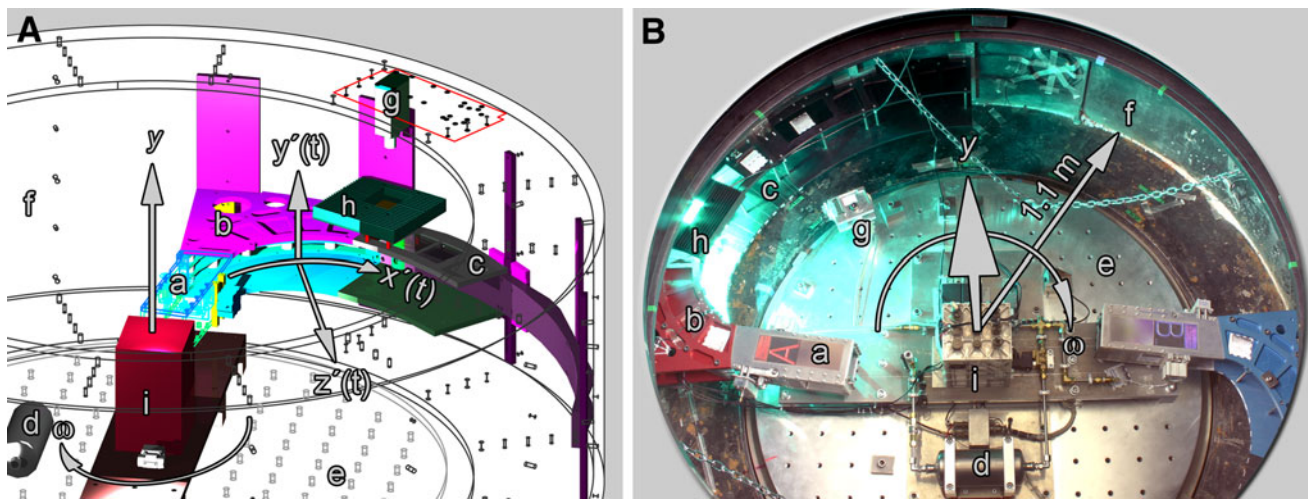
Fig. 5 a 3D Drawing of the experimental set-up: (*a*) hopper storing rock material pre-flight and releasing it in-flight; (*b*) acceleration chute; (*c*) run out chute segments; (*d*) compressed air tank for the pneumatic trap-door release system of the hopper; (*e*) tool plate; (*f*) drum; (*g*) high speed camera mounted vertically; (*h*) lighting system; (*i*) data acquisition box. The entire system rotates around the vertical *y*-axis in clock-wise direction with an angular velocity ω. The displacement of the experimental rock material is described by a moving coordinate system with the $x'(t)$-axis parallel to the channel base. **b** View into the drum centrifuge from top: For balancing and efficiency reasons the hopper and channel sections (*a*), (*b*), and (*c*) are mirrored. This allows performing two experiments during each run. The high speed camera (*g*) is shown on this image in an alternative, horizontal, mounting. The *outer radius* of the drum is 1.1 m; the hopper (*a*) is 12° inclined to radius of the drum; the acceleration channel (*b*) displays a radius of 0.325 m; and the run out channel (*c*) a radius of 1.06 m

Table 1 Quasi-static mechanical intact rock parameters of ETHAR

Property	Symbol	Unit	Value	Comment
Uniaxial compressive strength	$\sigma_{c,f}$	MPa	3.5($\pm$0.4)	[72]
Young's modulus	M	GPa	3.9($\pm$0.9)	[72]
Coefficient of restitution	COR	–	0.73($\pm$0.03)	[72]
Fracture surface energy	G_F	J/m^2	1.28($\pm$0.59)	[72]
Initiator size	r_0	mm	19, 32, 48	[72]

mal stress will act in the flow direction along the x'-axis. The intermediate normal stress will act horizontally, perpendicular to the flow direction along the y'-axis, where plane strain conditions may be assumed. The minimum normal stress, mainly due to the limited overburden of the rock mass, will act in the direction of the z'-axis.

During flow, the model material is loaded externally through an interplay of radial and tangential acceleration fields, and surface friction in the plus/minus y' and minus z'-directions, only. No other interaction between the model device and the sliding rock mass occurs, in contrast to ring shear apparatuses, which are also applied in sturzstrom research [41], where deformations are imposed on a rock material by a rigid plate boundary. A maximum velocity of about 15 m/s can be achieved in the x'-direction of the centrifuge model, allowing fully dynamic experiments to be performed. This maximum velocity is limited by the mechanical strength of the centrifuge apparatus, which is designed for a

440 times earth's gravity at a radius of 1.1 m, and is still about 5 times smaller than the estimated peak velocity of the Goldau sturzstrom in 1806 [51]. Preliminary centrifuge experiments revealed that the kinetic energies have been too low under such conditions to enable fragmentation of natural rock to occur through inter-particle collisions. A solution to this problem was to scale the strength of the rock material. For this reason, the ETH Analogue Material for Rock (ETHAR) was developed and applied in form of cubes with side lengths r_0 of 19, 32, or 48 mm. Data of ETHAR which are of interest here are given in Table 1. A detailed description and characterisation of that material, together with an analysis of its performance within the boundary conditions provided by this physical model environment, is discussed in [72].

A number of sensors are mounted on the model apparatus (Fig. 5) in order to monitor the experiment in flight (while the centrifuge is spinning) and to validate the analytically derived boundary conditions (Sect. 2.2.1).

2.2.1 The acceleration field

In any epistemologically thorough experiment, mastering the boundary conditions is crucial. The most important boundary condition of the centrifuge model is the acceleration field applied to the model material during the experiment. For a single point of mass, at time t, for a constant angular velocity ω of the centrifuge, the centrifugal acceleration $a_{r[cf]}(t)$, causing dislocation of the particle in the radial direction is defined by:

$$a_{r[cf]}(t) = \frac{v_{t,\text{channel}}^2(t - dt)}{r(t - dt)} \left[\text{m/s}^2 \right], \tag{1}$$

where $v_{t,\text{channel}}(t)$ is the tangential velocity of the channel at the radial position r of a particle. The centripetal acceleration $a_{r[cp]}(t)$ at time t that is forcing the mass point in a new radial trajectory is defined by:

$$a_{r[cp]}(t) = \frac{v_{t,\text{channel}}^2(t - dt) + v_t^2(t - dt)}{r(t - dt)}, \tag{2}$$

where $v_t(t)$ is the tangential velocity of a particle within the experiment. The tangential acceleration $a_{t[cp]}(t)$ at time t that is forcing the mass point in a new tangential trajectory is defined by:

$$\begin{aligned} a_{t[cp]}(t) \\ = 2 \cdot \frac{(v_{t,\text{channel}}(t - dt) - v_t(t - dt)) \cdot v_r(t - dt)}{r(t - dt)}, \end{aligned} \tag{3}$$

where $v_r(t)$ is the radial velocity of a particle within the experiment. The tangential velocity $v_t(t)$ at time t is defined by:

$$v_t(t) = v_t(t - dt) + a_{t[cf]}(t)dt, \tag{4}$$

and the radial velocity $v_r(t)$ at time t by:

$$v_r(t) = v_r(t - dt) + a_{r[cf]}(t)dt, \tag{5}$$

with the radial position $r(t)$ of the particle within the experiment at time t:

$$r(t) = r(t - dt) + v_r(t)dt + a_{r[cf]}(t)\frac{dt^2}{2}. \tag{6}$$

The last term in (6) describes the change in r during a time step dt. This term is omitted in the following solution because dt will be kept small.

These equations are solved iteratively. An example solution is presented in Fig. 6. This algorithm represents a single mass point solution which has been validated through single block centrifuge models [73]. Both the calculated accelerations and velocities can be seen as upper boundary values. Nevertheless, for the centre of mass of such a rock mass, this algorithm turned out to be reasonably accurate as long as the rock mass sliding behaviour can be described by a block frictional model. Still, this numerical model provides useful insight into the boundary conditions of a centrifugal model where mass points accelerate, decelerate and change their radial and tangential positions during the experiment rapidly (Fig 6).

2.3 Particle velocity

Videos taken with a high speed camera (Fig. 5a) revealed that the rock masses are sliding virtually as one block (Fig. 7), hence the differential velocities between the individual rock blocks are very small compared to the absolute sliding velocities of the rock masses tested. However, the rock mass experienced simple shear deformation in the x'-direction, which can be recognized by the distribution of layers of coloured rock blocks (Fig. 8a, b, c). The rock mass therefore moved, at least to a small degree, as a flow. This interpretation is discussed in more detail below. Another important observation is that, except for the very top layer in the z'-direction, the rock blocks do experience intensive fragmentation (Fig. 8c). The acceleration and velocity profiles (Fig. 6) show that the rock mass experiences strong slope parallel acceleration and subsequent deceleration in the direction of the x'-axis during the experiment. The acceleration field acts therefore as a virtual, soft "obstacle" capable of decelerating the rock mass rapidly. The effects interpreted from the image data (Figs. 7, 8) are that the rock mass experiences, due to inertial effects, shear displacements not only at the contact with the basal interface but also internally within the rock mass itself. Because the bottommost layers of the rock mass experienced the fastest deceleration, shear and collisional impacts of these rocks with the overriding hanging wall layers caused intensive fragmentation within this "process" zone. Further implications, which can be derived from these observations, are discussed in more detail below.

It should be noted that stresses generated by the artificial acceleration field alone turned out not to be sufficient to exceed the strength of the experimental rock material. This has been confirmed from a test set up where the extension of the rock mass was kept short in the x'-direction but constant in the z'-direction. Hence, the entire rock mass was sliding as one block and no fragmentation occurred. Thus, overburden pressure in the minus z'-direction can be ruled out as a cause of particle failure.

3 Fractal fragmentation

3.1 Fragmentation

The most striking result of the fracturing of rock particles within the centrifuge experiments is the fabric of the fragmented material achieved. Except for the approx. upper half of the deposit, which is only slightly fragmented, no parti-
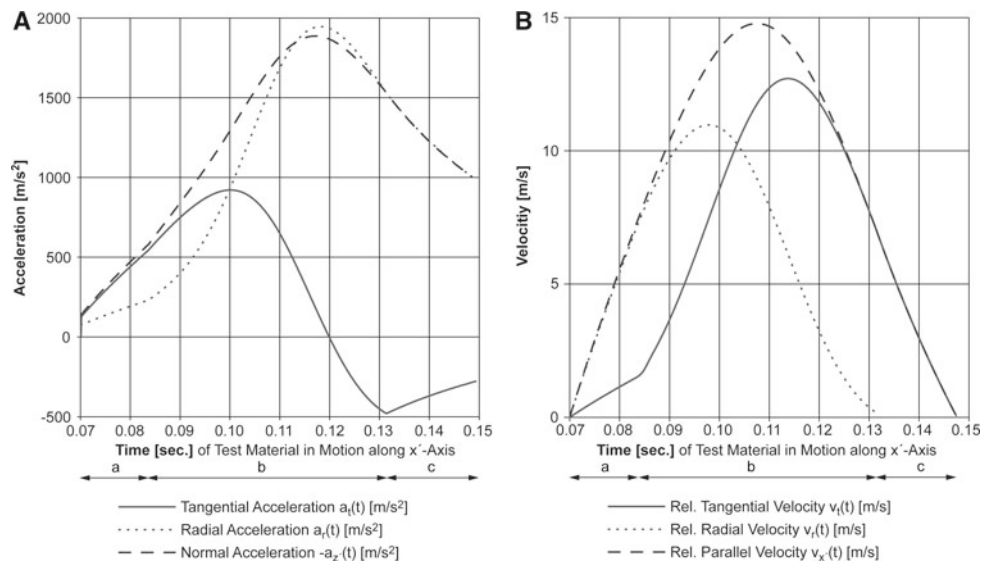
Fig. 6 Example of a numerical simulation of a centrifugal experiment at an angular velocity ω of the centrifuge of 30.4 rad/s, for the (*a*) hopper, (*b*) acceleration channel, and (*c*) run out channel sections. The experiment last for about 0.08 s. in total only. **a** Development of tangential, radial, and normal acceleration of the mass point during the experiment. The normal acceleration in the minus $z\prime(t)$-direction is responsible for the mobilization of frictional shear resistance between the mass point and the channel base. Note, that at the end of the experiment, when the mass point stopped, both the tangential and radial accelerations merge to a static acceleration of 1000 m/s². **b** Development of tangential, radial and channel parallel velocities of the mass point during the experiment relative to the channel base

cles of the same size were found in contact with each other (Fig. 8c). This observation is consistent with those made in nature, providing powerful evidence to validate this centrifuge model. The physical reasons for such a fabric are still under discussion. McDowell and co-authors [74–76] showed that the particle (tensile) strengths of single particles reduces as their size increases, whereas the works of [77,78] or [79] suggest that smaller particles "shield" larger particles and prevent their failure by distributing the loading over them. Therefore particles of similar size in contact with each other are more likely to fail than those of different sizes. In the present case, where particles are loaded dynamically, an additional process may be effective in causing fragmentation: that of momentum transfer. From this point of view, only particles of a similar size that collide with each other, or small particles impacting large ones, or being impacted by large ones, will fragment. This process will also lead to larger particles floating in a matrix of finer ones.

3.2 Particle size distribution

Comparing the particle size distributions achieved in the centrifugal experiments (Fig. 9a) with the distributions revealed by sieving samples of deposits of true sturzstroms (Fig. 9b), provides insight. If the size distribution of the particles of a rock mass is proportional to a power law relation with the slope υ, where:

$$N\left(r \geq R\right) \propto R^{-\upsilon}, \tag{7}$$

then a fractal is defined [80–82]. R is a measure of length (e.g. sieve aperture) in this equation, $N\left(r \geq R\right)$ is the cumulative number of particles with a length $r \geq R$. The fractal dimension D can be calculated from the relationship given in (7) as:

$$D = 3 - \upsilon\left[--\right], (e.g.[81]). \tag{8}$$

However, due to practical reasons, it is typical to work with the percentage of cumulative mass of particles m of size r "less than" R— $m(r < R)$, because measurements are obtained directly from sieve analyses. Under the assumption of uniform particle density, Tyler and Wheatcraft [82] showed that a valid and robust way of obtaining the mass based fractal dimension D from real sieve data, is to regress $m(r < R)$ on R expressed in the log/log space according to the power law relation:

$$m\left(r < R\right) = kR^{\upsilon}, \tag{9}$$

where k, is the offset of the regression line.

Turcotte [81] developed the proposition that D is sensitive to a particular mode of fragmentation. Hence comminution processes can be interpreted and compared in terms of D. To perform such a comparison, the deposits of the centrifuge experiments have been collected and dry sieved carefully by hand (e.g. [83]) to reveal their cumulative mass–particle size distribution. The samples from the Flims, Grächen, Goldau

Fig. 7 View into the "A" channel of the model. Image taken by the black and white high speed camera during the experiment. The arrow indicates the flow in the x'-direction and serves as a scale. Its length is 32 mm, which equals the initial side length r_0 of the intact blocks. The rock blocks remain in contact during the entire experiment. This simulation was performed at an angular velocity ω of the centrifuge of 30.4 rad/s

and Köfels sturzstroms (e.g. Sect. 1) have been examined in the same fashion. These data are plotted in Fig. 9b. Within the two orders of magnitude of r for these data, D ranges from 2.60 to 2.86. These values of D obtained from the centrifugal experiments fit well to the fractal dimensions of the Grächen, Goldau and Köfels sturzstroms, but not to those of Flims. They are also in the range of values of D for other natural sturzstroms also, as presented in the data compiled by Crosta et al. [84] for particles with r up to 1000 mm. Another interesting observation for this centrifuge experiment in particular is that most of the slopes of the cumulative mass-particle size distributions tend to decrease (while D increases) for particles with $r < 8$ mm, which may be interpreted as a change in the mode of fragmentation.

3.3 Comminution model

What insights can be gained from the fractal dimensions derived, and what are the underlying comminution processes? Sammis and co-authors [77,85] presented an idealised, deterministic comminution model (Fig. 11), with a cumulative mass–particle size distribution yielding a D of 2.58. Fig. 9b shows that this model resembles the cumulative mass-particle size distributions of the Flims sturzstrom to a good degree, as well as the "mean" of all other mass-particle size distributions, for particles with $r > 8$ mm. Data of the cumulative mass-particle size distribution for particles with $r > 32$ mm have not been collected for this study, but data from literature indicate a sufficient fit to this comminution model [84,86].

The "initiator" [80] of the comminution model by [77] is a cube with an initial side length of r_0. The mass conserving "generator" operation retains at each cycle or scale, diagonally opposed blocks, but fragments others. The result is that no blocks of equal size are in direct contact with each other (Fig. 10). The net number of blocks N_n that are newly created
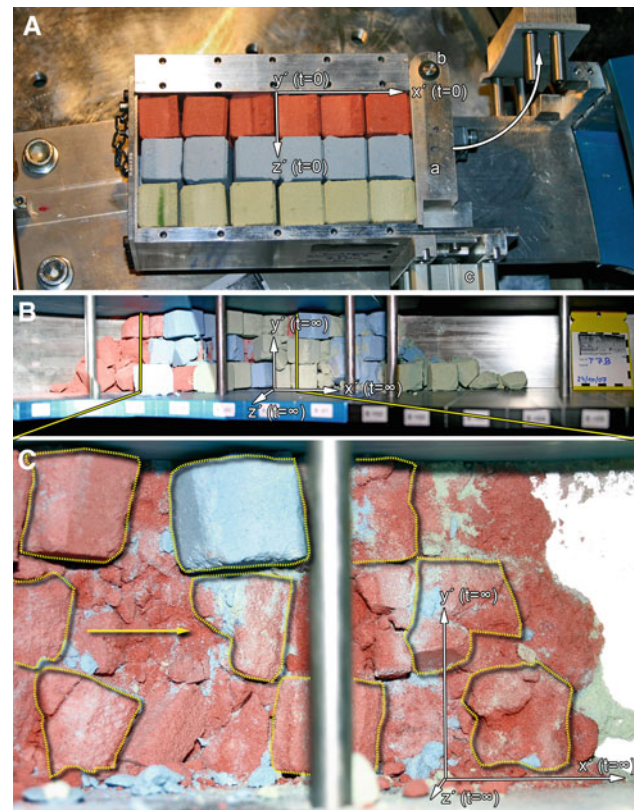

Fig. 8 A characteristic example of the internal deformation of the rock "flow" simulated within the centrifugal experiment. This simulation was performed at an angular velocity ω of the centrifuge of 30.4 rad/s. **a** The hopper section of the experiment (cover lid removed). (*a*) trap door and its hinge (*b*); (*c*) pneumatic piston to unlock the door in-flight. The hopper is filled in the positive z'-direction with layers of *red*, *blue*, and *green* rocks. **b** View into the acceleration and run out channels of the model showing a total view of the rock "flow" deposit at the end of the experiment. As depicted in Fig. 7, the rock blocks remain in contact during the entire experiment. Beside that, the rock mass experiences internal deformation by simple shear during run out, resulting in a relative displacement of the layers of *coloured* rocks. The *red*, *bottommost*, foot-wall layer stopped first, forming now the proximal end of the deposit in the minus x'-direction. This layer has been partly overrun by the hanging-wall *blue* and *green layers* whereas the *uppermost green layer* stopped last, forming now the distal toe of the deposit in the plus x'-direction. The distortion of the proximal and distal ends of the deposit originates from gravity acting in the minus y'-direction which becomes significant post-flight when the centrifuge has been stopped. **c** Magnification of the rock "flow" deposit but with the approx. upper half, in z'-direction of the rock mass, stripped. Whereas the uppermost rock blocks remained widely intact, the bottommost layer displays intensive fragmentation. The *dotted lines* mark the perimeter of $\pm$ intact blocks still existing in that matrix supported deposit. The *arrow* indicates the flow in the x'-direction and serves as a scale with a length of 32 mm, which equals the original side width r_0 of the rock blocks applied in this experiment

during a cycle n, can be calculated as:

$$N_n = 8 \cdot 6^{n-1}. \tag{10}$$

The usefulness of this model is that it allows the quantitative description and prediction of key parameters necessary for understanding the energy budget of sturzstroms. In the view
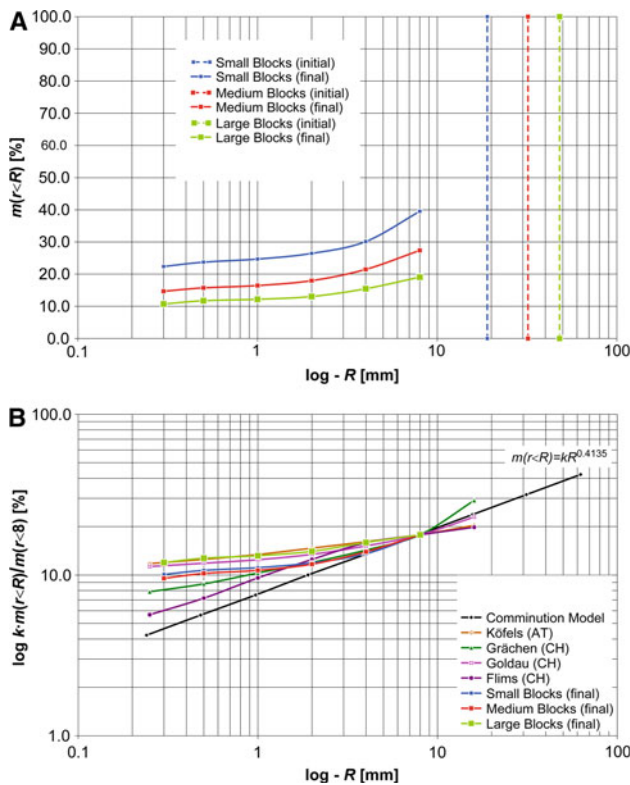
Fig. 9 a Initial and final cumulative mass particle size distributions $m(r < R)$ resulting from the centrifuge experiments performed at an angular velocity ω of 31 radians/s, utilizing blocks of ETHAR with initial dimensions r_0 of 19 mm (small), 32 mm (medium), and 48 mm (large). The final cumulative mass particle size distributions comprise fines $\leq$ 8mm, which can be determined from standard sieve analysis, only. Larger particles represent either non- or only partially fragmented blocks. **b** Cumulative mass particle size distributions, normalized over a constant offset k at $R = 8$ mm, for various sturzstroms, compared with the results from the centrifuge experiments and the synthetic grain size distribution calculated from the comminution model after [77]. The change in slope for most particle size distributions below approx. 8 mm may indicate a change in the comminution mode

of the model, fragmentation changes from a continuous to a periodic process, hence the fragmentation of the initiator occurs in cycles. In order to calculate the energy dissipated by the formation of new fracture surfaces, the net surface area A_n, which is newly formed during a cycle n, is calculated as:

$$A_n = \frac{3^n}{2^{n-1}} \cdot r_0 [m^2]$$ (11)

4 Dispersive stress model

The fragmentation–spreading model of sturzstroms after Davies, McSaveney and co-authors [23,46–50,86,87] is based on the violent phenomenon of "rock bursts" [88–90]. The micro-mechanics of rock burst is still under debate. But in a general sense, bursts occur when quasi-brittle rocks are

loaded up to their failure strength. In that case their stored elastic strain energy is partly recovered as kinetic energy of the failed particles, which acts predominantly in the direction of the minimum effective principal stress σ'_3 (Fig. 11). Thus a dispersive stress or "granular pressure" [87] $\sigma_{disp,n}$ may evolve from such a cloud of failed rock particles, reducing effective stresses in the minus z-direction and hence frictional resistance τ_x mobilised within the sturzstroms:

$$\tau_{x,n} = \left(-\sigma_z + \sigma_{disp,n}\right) \cdot \mu,$$ (12)

This expression allows the dispersive stress concept to be combined with the effective stress concept by [91] and the Coulomb frictional model, where the friction coefficient is denoted as μ.

The elastic strain energy $E_{elas,f}$ stored just before failure may be calculated for a triaxial principal stress state, during a cycle n, utilizing the comminution model presented here, as (modified after [92]):

$$\begin{aligned} E_{elas,f,n} = \frac{1}{2M} \cdot \Big(& \sigma'^2_{1,f} + \sigma'^2_{2,f} + \sigma'^2_{3,f} - 2 \cdot \upsilon \cdot \\ & \left(\sigma'_{2,f} \cdot \sigma'_{3,f} + \sigma'_{3,f} \cdot \sigma'_{1,f} + \sigma'_{1,f} \cdot \sigma'_{2,f}\right) \Big) \\ & \cdot r^3_n \cdot N_n, \end{aligned}$$ (13)

where M denotes the small strain elastic modulus, $\sigma'_{1,2,3,f}$ the effective principal stresses at failure and N the number of particles affected.

The energy dissipated by fragmentation E_{frag} can be calculated for a cycle n as:

$$E_{frag,n} = A_n \cdot G_F,$$ (14)

where G_F denotes the fracture surface energy [69,72]. The dispersive kinetic energy E_{disp} released at failure may be calculated for a cycle n as:

$$E_{disp,n} = E_{elas,f,n} \cdot COR - E_{frag,n},$$ (15)

where COR denotes an elastic coefficient of restitution of rock [93].

4.1 Mechanical rock properties

At this point, it is necessary to consider the fracture surface energy G_F going into (14), and the compressive strength of rock, which will affect the principal yield stresses $\sigma'_{1,2,3,f}$ (13), in more detail. Although the mobilized strength (among others [94–96]) and the elastic properties of rock may vary with strain rate it was deliberately decided not to endeavour to consider any dynamic properties at the present stage of the work. The first reason is that estimating strain rates generated between colliding rock particles in a true sturzstrom with any accuracy would be extremely difficult in practice, because a very wide range of particle sizes occur in sturzstroms, which are interacting with each other on very irregular interfaces.
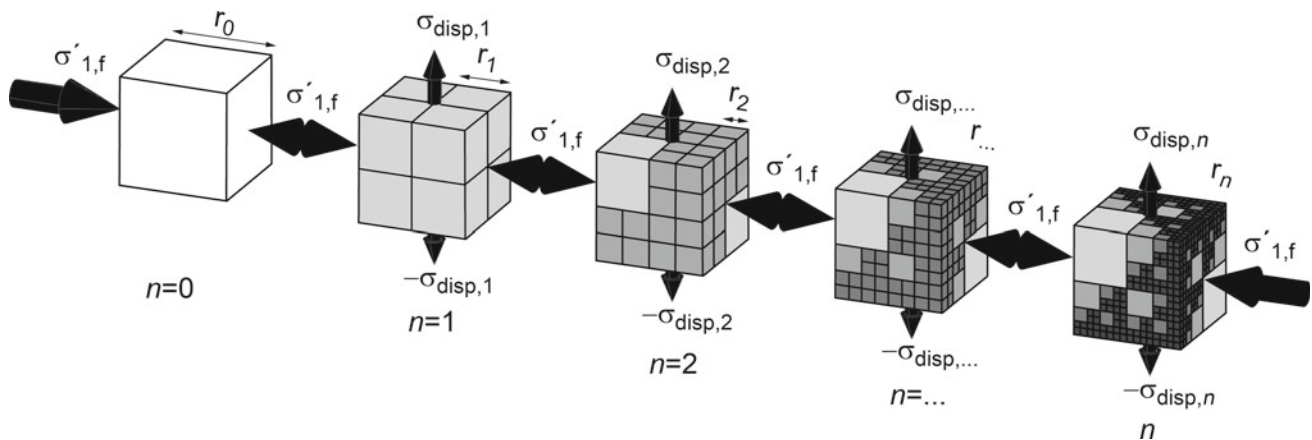
Fig. 10 An idealized, deterministic model for fractal fragmentation after [77]. A zero order cubic cell with the dimension r_0 is divided into eight cubic elements with dimensions of $r_n = r_{n-1}/2$. This process is repeated to higher orders whereas two diagonally opposite cubes are retained at each scale. The basic structure is fractal yielding a D of 2.58. $\sigma'_{1,f}$ symbolise the maximum effective principal stress at failure. $\sigma'_{disp,n}$ symbolise the dispersive stresses at failure in the direction of the minimum effective principal stress $\sigma'_{3,f}$
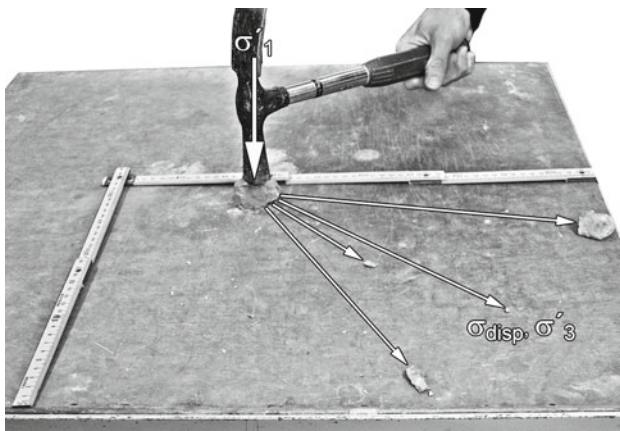

Fig. 11 Hitting a rock block with a hammer: conversion of kinetic energy into elastic strain energy and reconversion of the elastic strain energy into kinetic energy after failure of the rock. An interesting effect of fragmentation is that the maximum effective principal stress σ'_1 is deflected quasi-perpendicular, in direction of the minimum effective principal stress σ'_3. The resulting cloud of particle fragments may then induce a load on surrounding particles, which will cause a dispersive stress σ_{disp}. The behaviour of quasi-brittle rocks [72] within this very simple experiment can be confirmed, by any standard laboratory compressive strength test

Estimates of dynamic rock properties may therefore rather contribute to indeterminacy than to solving problems. The second reason is that the tremendous geometric irregularity of rock particles forming sturzstroms may have a higher influence on their mechanical behaviour than strain rates do (among others [75,92]), but this dependency can be incorporated in an analysis more simply.

Taking quasi-static mechanical rock properties of the "Bunte Rigi-Nagelfluh" conglomerate, the predominant rock constituting the Goldau sturzstrom of 1806 as an example (Table 2, [72]), and assuming in the first instance that the mechanical properties are independent of particle size

(Fig. 12a), the balance between $E_{frag,n}$ and $E_{disp,n}$ available is depicted in Fig. 12b. In this case, the development of $E_{frag,n}$ would serve as a stopping criterion for the mechanical fluidization of a sturzstrom because all elastic strain energy $E_{elas,f}$ available would be dissipated in fragmentation energy. Taking $3.5 \cdot 10^7 \mathrm{m}^3$ as the volume of the Goldau 1806 sturzstrom [51], and assuming an initial rock block side length r_0 of 1 m, it can be estimated for constant mechanical rock properties, that approx. $2 \cdot 10^8$ MNm of E_{frag} may be consumed to comminute that rock mass down to a particle size of $1 \cdot 10^{-5}$ m. This amounts to approx. 1/3 of the potential energy available within that event, based on the fall height of its centre of mass of about 700 m [51]. This value lies close to the estimations reported in [97]. In this case, fracturing would constitute, beside friction, a significant energy sink within the energy budget of sturzstroms.

Assuming a dependence of G_F and $\sigma_{c,f}$ from the particle size r_n, a different picture evolves. $G_{F,n}$ may vary, based on the input parameter shown in Table 3, according to:

$$G_{F,n} = k_{G_F} \cdot r_n^{\alpha_{GF}} \Rightarrow k_{G_F} \cdot \left(\frac{r_0}{2^n}\right)^{\alpha_{GF}}, \qquad (16)$$

based on a power law regression of data presented in [98] with $\alpha_{GF} \sim 0.4$ as its slope (Fig. 12c). The offset k_{G_F} is calculated in the present case for a characteristic specimen dimension r of 1 m (e.g. [98]) as:

$$k_{G_F} = r^{-\alpha_{GF}} \cdot G_F \Rightarrow 1^{-0.4} \cdot 400 = 400 \left[\mathrm{J/m}^2\right]. \qquad (17)$$

The particle size dependence of $\sigma_{c,f,n}$ may be described as (Fig. 12c):

$$\sigma_{c,f,n} = k_{\sigma_{c,f}} \cdot r_n^{-\alpha_{\sigma,c,f}} \Rightarrow k_{\sigma_{c,f}} \cdot \left(\frac{r_0}{2^n}\right)^{-\alpha_{\sigma,c,f}}, \qquad (18)$$

based on data from the literature for uniaxial compression [92] and also for tensile particle splitting [75]. According to

Table 2 Quasi-static mechanical intact rock parameters of the "Bunte Rigi-Nagelfluh" conglomerate

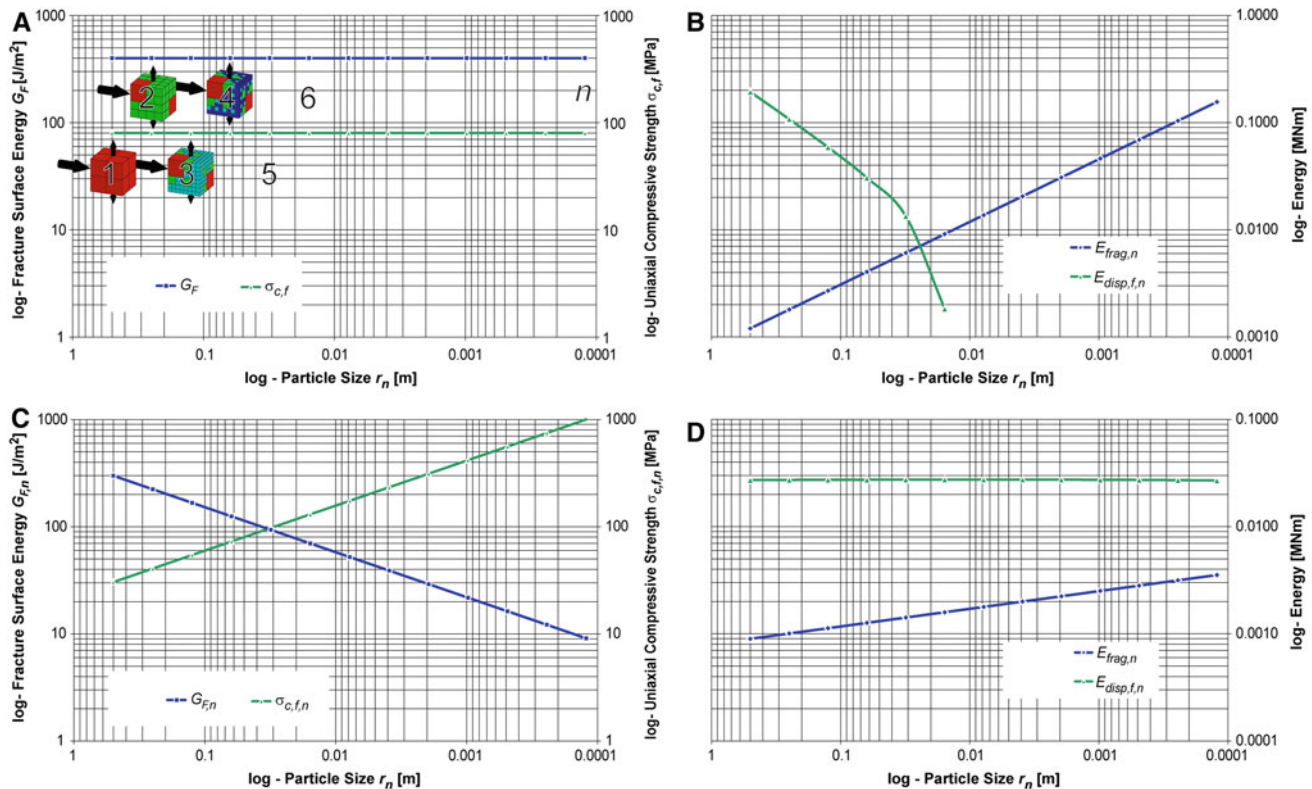| Property	Symbol	Unit	Value	Comment
Uniaxial compressive strength	$\sigma_{c,f}$	MPa	84($\pm$19)	[51,72]; specimen diameter 0.05 m
Young's modulus	M	GPa	18($\pm$4)	[72]; specimen diameter 0.05 m
Coefficient of restitution	COR	–	0.89($\pm$0.01)	[72,93]
Fracture surface energy	G_F	J/m^2	400	estimation after [98] for characteristic specimen size of 1 m
Initiator size	r_0	m	1.0	

Fig. 12 **a** Assumption of a particle size independence of the fracture surface energy G_F and uniaxial compressive strength $\sigma_{c,f}$. **b** The increase of newly created fracture surfaces (11) causes that after a few cycles n, the energy necessary to create new fracture surfaces $E_{frag,n}$ (14), exceeds the elastic strain energy $E_{elas,f,n}$ (13), which sharply reduces the dispersive strain energy $E_{disp,n}$ (15) available. In this case, the development of $E_{frag,n}$ would serve as a stopping criterion for the mechanical fluidization of a sturzstrom because all elastic strain energy $E_{elas,f}$ available would be dissipated in fragmentation energy. The energies in this example are calculated for a volume of 1 m^3 of rock with an initial side length r_0 of 1m. **c** Assumption of a particle size dependence of G_F (16) and $\sigma_{c,f}$ (18). The development of $\sigma_{c,f}$ would serve as stopping criterion for the mechanical fluidization of a sturzstrom because the particles will reduce in size and therefore become too strong to experience further fragmentation within the collisional environment of a sturzstrom. **d** The particle size dependent decrease of G_F causes only a gentle increase in energy necessary to create new fracture surfaces $E_{frag,n}$ (14). The energies in this example are calculated for a volume of 1 m^3 of rock with an initial side length r_0 of 1 m

these data, the slope $\alpha_{\sigma,c,f}$ of the power law regression can also be set to 0.4. This is not surprising because both the uniaxial compression and, as the name already says, the tensile splitting test, cause the formation of mode I tensile cracks within the material tested. The offset $k_{\sigma,c,f}$ is calculated in the present case for a specimen diameter r of 0.05 m as:

$$k_{\sigma_{c,f}} = r^{0.4} \cdot \sigma_{c,f} \Rightarrow 0.05^{0.4} \cdot 84 = 25.3 \,[\text{MPa}] \,. \qquad (19)$$

The resulting balance between E_{frag} and E_{disp} is depicted in Fig. 12d. The development of $\sigma_{c,f}$ would serve as stopping criterion for the mechanical fluidization of a sturzstrom because the eventually small particles would become too strong to experience further fragmentation within the collisional environment of a sturzstrom (Fig. 12c). Again, taking $3.5 \cdot 10^7 \text{m}^3$ as the volume of the Goldau sturzstrom [51] and assuming an initial rock block size r_0 of 1 m, it

can be estimated for this case, that approx. $2 \cdot 10^6$ MNm of E_{frag} may be consumed to comminute that rock mass down to a particle size of $1 \cdot 10^{-5}$ m. This would not even be 1% of the potential energy available. In this case, fracturing would constitute an almost negligible energy sink within the energy budget of sturzstroms. Estimations yielding such a low value have also been reported by [50].

Of these two simple examples, the second, non-linear, particle size dependent case, is more realistic, because it is closer to empirical evidence. But it is clear that this assumption still does not cover all concerns that arise around the complex field of fracture mechanics. Turcotte [99] concludes: "Fragmentation involves the initiation and propagation of fractures and is a highly non-linear process requiring complex models even for the simplest configuration." This must be even truer for combining fragmentation with sturzstroms. The indeterminacy of the given problem calls for a focus on a few, established properties. This is thought to be far more useful than to give undue emphasis to the intricacies of a particular theory or approach (e.g. [100]). Therefore it was decided not to explore the influence of fracture mechanics any further within this contribution.

5 Discussion

5.1 Effects of the dispersive energy

A more immediate approach than attempting to calculate a dispersive stress σ_{disp} is to take the post failure kinetic energy of the fragmented particles to analyze the influence of fragmentation on the emplacement of sturzstroms. This is done by implementing (11) and (13–19) within a distinct element model (DEM). This code models the movement and interaction of assemblies of rigid spherical particles, which is performed by an alternating calculation of Newton's second law of motion and a force-displacement model at the contacts. A detailed description of this DEM is given by [12,14]. A simple linear contact model, with the possibility for representing energy dissipation by elastic hysteretic damping and frictional slip, has been adopted as force-displacement constitutive relation for the present research project. Such a numerical description offers the possibility to describe a granular medium, like a sturzstrom, via a "granular", iterative comminution model, within a "granular" DEM. This DEM may simulate fragmentation of bonded rigid spheres numerically. These bonds would fail if their strengths would be exceeded either in the normal or shear directions. Representing rock in this way, in order to model shear localization, was successfully applied by [101,102], for example. The drawback of such a formulation is that it would require small rigid model spheres (in the range of centimetres or smaller) to

simulate the behaviour of real intact rock successfully. This would limit, with the computational power available today, the true model volume within a range of much smaller than one cubic metre.

The elegance of the solution presented here is to apply the comminution model after [77] within the continuum of a rigid sphere itself to allow for its "virtual" fragmentation. Such a formulation enables the usage of larger, unbonded particles and, eventually, the simulation of sturzstroms at true scale.

The post failure, dispersive kinetic energy is now considered within the DEM by letting a dispersive velocity $v_{disp,n}$ acting on a single rigid particle of mass $m_{particle}$, in the direction of σ'_3 (Fig. 13):

$$v_{disp,n} = \sqrt{\frac{2 \cdot E_{disp,n}}{m_{particle}}} \ [\text{m/s}], \tag{20}$$

if the three dimensional deviator stress q' [103]:

$$q' = \frac{1}{\sqrt{2}} \cdot \left[\left(\sigma'_{1,f} - \sigma'_{2,f} \right)^2 + \left(\sigma'_{2,f} - \sigma'_{3,f} \right)^2 \right.$$
$$\left. + \left(\sigma'_{3,f} - \sigma'_{1,f} \right)^2 \right]^{1/2} \ [\text{MPa}], \tag{21}$$

exceeds $\sigma_{c,f,n}$ (18). The input average normal and shear stress tensor $\bar{\sigma}_{ij}$ of a particle (p) is calculated as:

$$\bar{\sigma}_{ij}^{(p)} = -\frac{1}{V^{(p)}} \cdot \sum_{N_c} \left| x_i^{(c)} - x_i^{(p)} \right| \cdot n_i^{(c,p)} \cdot F_j^{(c)}, \tag{22}$$

where V is the volume of the particle, N_c the number of particle/particle or particle/ground contacts acting on (p), $x_i(p)$ and $x_i(c)$ are the locations of the particle centroid and its contacts, n_i is the unit normal vector directed from a particle centroid to its contact location and F_j is the force acting at a contact (c) [11,12]. The magnitudes and the directions of the principal stresses $\sigma'_{1,f}$ and $\sigma'_{3,f}$ of particles undergoing fragmentation are calculated from (22) as the eigenvalues and eigenvectors of the stress tensor $\bar{\sigma}_{ij}$ (Figs. 13, 14).

Exploring the full potential of the DEM applied would exceed by far the purpose of the current study. Therefore, two simple examples will be shown to highlight the effects of dynamic fragmentation on fast moving rock masses like sturzstroms. The simulations shown consist of a rock mass block with a volume of $1 \times 10^7 \text{m}^3$ (Goldau $\sim 3.5 \times 10^7 \text{m}^3$) consisting of $\sim$10000 unbonded rigid particles. The size ratio r_{max}/r_{min} of the rigid particles numbers 1.86 to prevent a reorganisation of the particles within a closed-packed lattice, which otherwise would dramatically alter the behaviour of the particle assembly [102]. The number of "initiators" $N_{initiator}$ of the comminution model by [77], with a side length r_0 and a volume $V_{initiator}$, which lie within a single rigid particle with a diameter $r_{particle}(r_{min} \leq r_{particle} \leq$

Table 3 Quasi-static, particle size dependent, mechanical intact rock parameters

| Property	Symbol	Unit	Value	Comment
Fracture surface energy	G_F	J/m^2	400	Estimation after [98] for characteristic specimen size of 1 m
Offset G_F	k_{GF}	J/m^2	400	
Slope G_F	α_{Gf}		0.4	e.g. [98]
Uniaxial compressive strength	$\sigma_{c,f}$	MPa	84	[51,72]; for specimen diameter 0.05 m
Offset $\sigma_{c,f}$	$k_{\sigma,c,f}$	MPa	25.3	
Slope $\sigma_{c,f}$	$\alpha_{\sigma,c,f}$		0.4	e.g. [75]
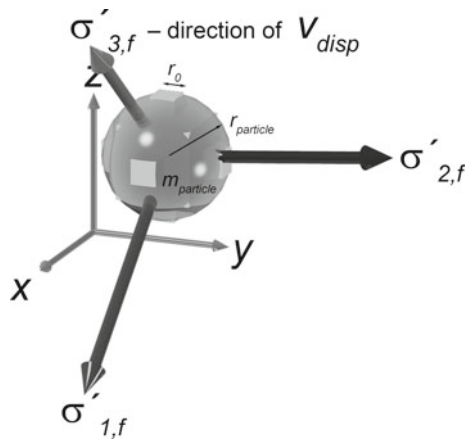
Fig. 13 Rigid particle of the DEM with mass m$_{particle}$, located within a cartesian coordinate system with the *x*-axis parallel to the flow of the simulated sturzstrom. The particle is loaded by the three prinicipal stresses $\sigma_1' > \sigma_2' > \sigma_3'$. If the deviatoric stress q' (21) exceeds $\sigma_{c,f}$ (18), a dispersive velocity v_{disp} (20) is applied in the positive direction of σ_3'. The number of "initiators" $N_{initiator}$ of side length r_0, which fits into the volume of the rigid particle of radius $r_{particle}$ is calculated by (23)

r_{max}) and a volume $V_{particle}$ (Fig. 13) is calculated as:

$$N_{initiator} = \frac{6}{8} \cdot \frac{V_{particle}}{V_{initiator}} \Rightarrow \frac{6}{8} \cdot \frac{\left(\frac{4}{3} \cdot r_{particle}^3 \cdot \pi \right)}{r_0^3}. \quad (23)$$

Note that $N_{initiator}$ does not need to be an integer number and that only 6 blocks of an initiator split into 8 blocks (e.g. (10) for $n = 1$ and Fig. 10), hence 75% of $V_{particle}$ will experience further fragmentation according to the comminution model. The comminution model is now applied to every rigid particle of the DEM by multiplying (14) and (15), and (13) with $N_{initiator}$.

This particle assembly in the examples is defined to move on a completely flat floor with an initial velocity of 70 m/s (according to maximum velocities proposed for Goldau [51]). Two DEM simulations, case I (Fig. 15) and case II (Fig. 16), will be compared in their run-out behaviour. Their primary input parameters are presented in Tables 2, 3, and 4. The only variation between case I and II will be
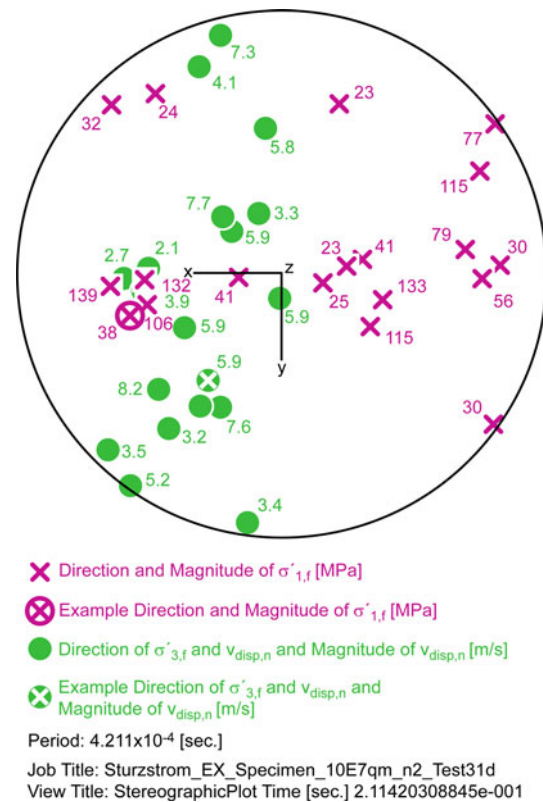
Fig. 14 Example of sturzstrom simulated within the DEM consisting of 10000 rigid particles. The orientation of principal stresses $\sigma_{1,f}'$, $\sigma_{3,f}'$ and $v_{disp,n}$ of particles under failure are plotted in an isogonal, stereographic projection during a period of 4.211^{-4} s at 0.21 s after simulation starts. It can be seen that the maximum principal stresses are rarely oriented in the z'-direction. The overburden pressure is therefore smaller than the normal and shear stresses acting in the sub x'-direction. One rigid particle (Fig. 13) is indicated to serve as an example. Its maximum principal stress $\sigma_{1,f}'$ numbers 38 MPa and displays a trend of 344° (in clockwise direction with the *x*-axis as zero) and a plunge of 40°. Its minimum principal stress $\sigma_{3,f}'$ is oriented perpendicular to $\sigma_{1,f}'$ and displays a trend of 305° and a plunge of 50°. $v_{disp,n}$ acts in the same direction as $\sigma_{3,f}'$ and is 5.9 m/s in this example

the friction coefficient μ mobilized in the interface particle assembly/ground, which is considerably higher in case II.

The run-out behaviour of case I is depicted in Fig. 15. All particles move as a flexible sheet due to the relatively low
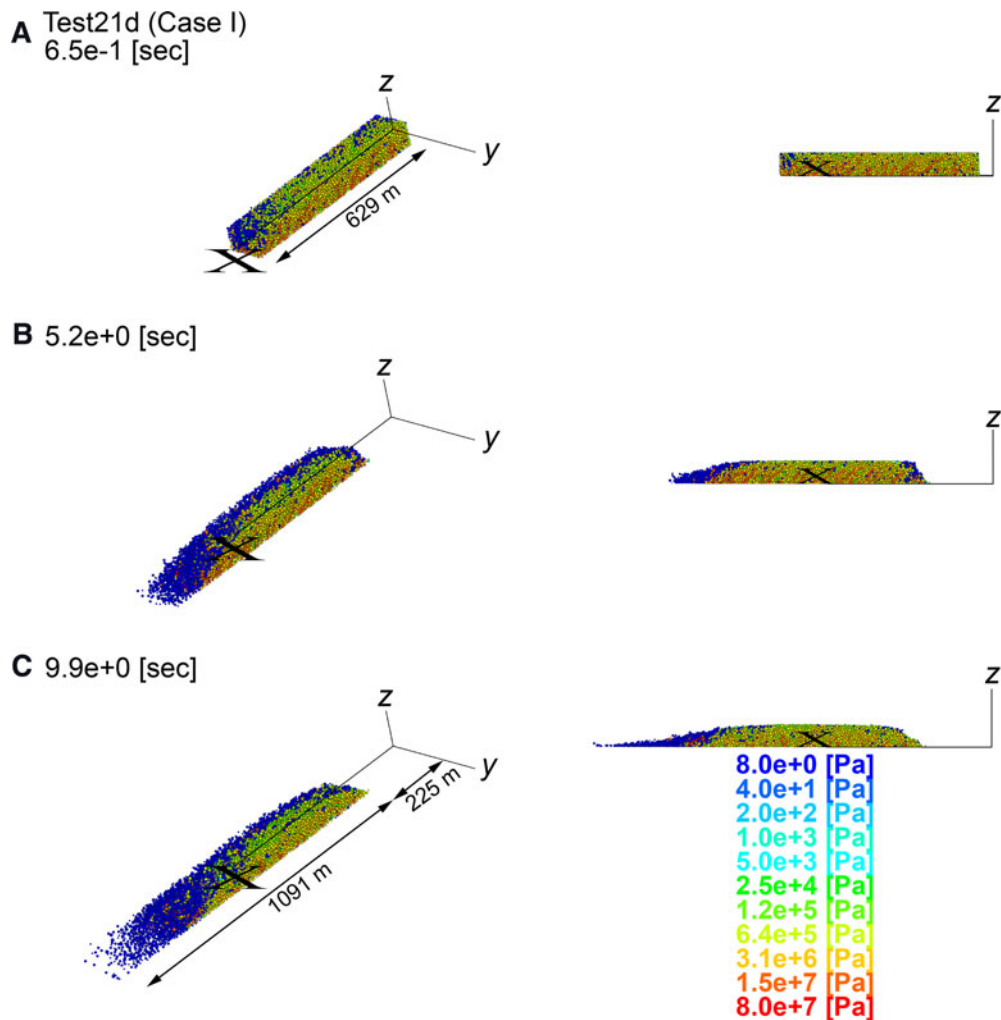
Fig. 15 Simulation of a rock mass block with a volume of $1 \times 10^7 \text{m}^3$ consisting of ∼10000 rigid particles moving with an initial velocity of 70 m/s in the x-direction. The initial dimensions are $x = 629.46$ m, $y = 209.82$ m, $z = 75.72$ m. Only the right half ($y/2$) from the total assembly is shown. The *colour coding* of the particles indicates their deviator stress q' state. The friction coefficient mobilized by the ground $\mu_{ground,I}$ is set to 0.5 (Table 4). Gravity is acting in the minus z-direction. **a** Initial particle assembly. **b** Particle assembly at the halftime of the total simulation duration. **c** Final particle assembly with all velocities <0.1 m/s

frictional resistance at the base, showing very low relative displacements between the particles. This results in a low stress level within the particle assembly, causing very few particles to reach their yield strength and to fragment. The lack of dispersive stress within the particle assembly causes it to move and to stop, as it would be predicted by a simple frictional block model. Only inertial effects cause the front of the particle assembly to spread slightly (Fig. 15c).

Figure 16 shows the run-out behaviour of case II, whereby the high friction mobilized along the ground causes particles in contact with the floor to decelerate rapidly compared to the rest of the particle assembly (Fig. 16a). The result is that the zone of highest shear displacement migrates from the

ground into the particle assembly itself (Fig. 16b, c). In this shear zone the relative velocities between the particles are so high that stresses sufficient to yield fragmentation occur. As soon as this is the case, the dispersive stresses cause a dilation of the particle assembly with a simultaneous reduction of the shear resistance that can be mobilized in the shear zone. The particle assembly above the shear zone may now override the material below the shear zone (Fig. 16b, c). High dilation and low shear resistance are at the same time the reason for fragmentation and the development of dispersive stresses to cease—which lays the ground for high shear stresses to be mobilized again—a new cycle of fragmentation. The resulting spreading is much more prolonged than in case I.
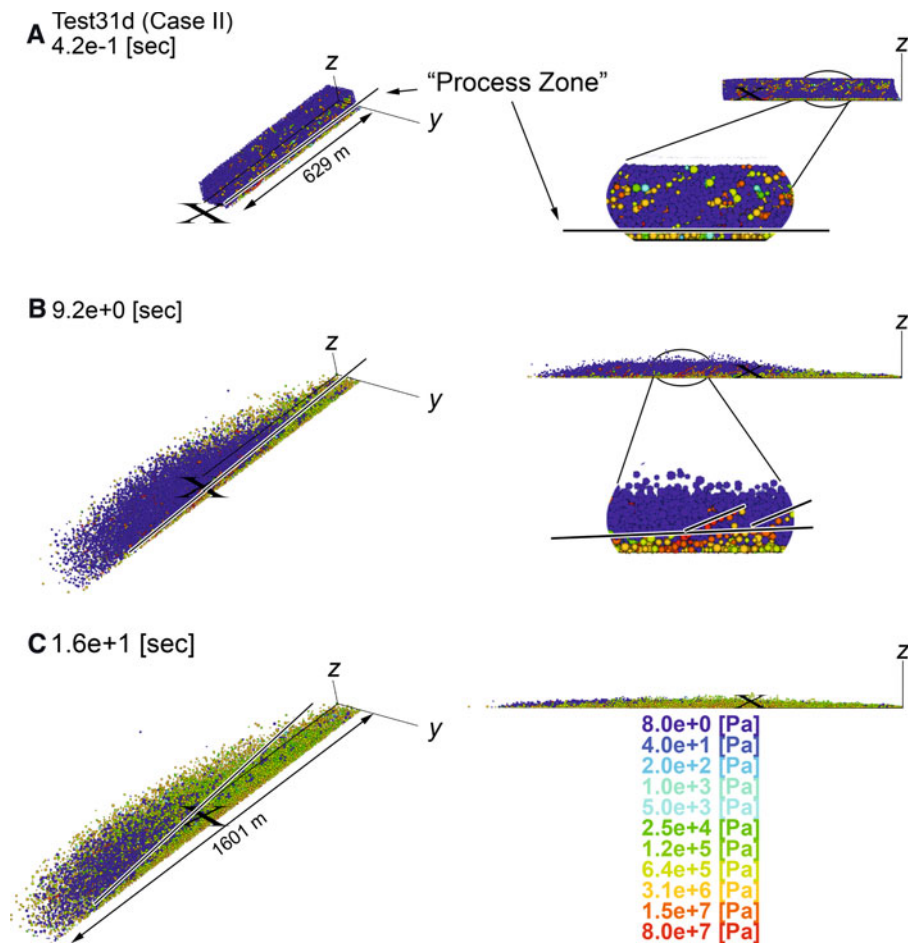
Fig. 16 Simulation of a rock mass block with a volume of $1 \times 10^7 \mathrm{m}^3$ consisting of ~10000 rigid particles moving with an initial velocity of 70 m/s in the x-direction. The initial dimensions are $x = 629.46$ m, $y = 209.82$ m, $z = 75.72$ m. Only the right half ($y/2$) from the total assembly is shown. The *colour coding* of the particles indicates their deviator stress q' state. The friction coefficient mobilized by the ground $\mu_{ground,I}$ is set to 9.5 (Table 4) representing "rugged" ground. Gravity is acting in the minus z-direction. **a** Particle assembly 0.42 s after simulation starts. The particles coloured in *blue* indicate a practically stress free, dispersed zone of the assembly where all particles move at the same velocity within a granular "cloud". The reason for this can be found at the base, where particles in contact with the ground have been decelerated dramatically forming a "process zone" displaying high shear strain, stress and fragmentation (enlarged detail). **b** Particle assembly at the halftime of the total simulation duration. The dispersed assembly collapses, forming new "process zones" in which particle fragmentation will cause dilatancy of the assembly again (enlarged detail). **c** Final particle assembly with all velocities <0.1 m/s. It can be seen that the "process zone" migrated from the ground all the way to the very top "layer" of the particle assembly which, is still, at that time of the experiment, in a highly dispersed state, indicated by the *blue* colouring of the particles

5.2 Inertial entrainment friction

The assumption of a very high friction coefficient at the base, as in case II, is reasonable, describing an "apparent" friction postulated as a concept of "inertial entrainment friction". This concept is developed based on own observations and literature that sturzstroms "and their deposits reflect strong interactions with rugged terrain and deformable, wet substrates" [104]. A terrain may not only be considered as "rugged" due to the presence of obstacles, where a high "apparent" friction seems obvious, it could also apply to completely flat terrain in soft soil, in which material will be entrained by ploughing (Fig. 17). In consequence it may be assumed that every rock block in contact with the basal soil will accelerate a volume of soil of the same or even higher mass than the mass of the block itself. The result is that at the base of a sturzstrom, not only the drained or undrained internal frictional resistance of the soil has to be overcome, but also the momentum of the rock particle is transferred into the ground. This causes the basal layers of rocks to be decelerated dramatically compared to the rock mass above. The result is that the zone of the highest shear displacement will migrate upwards into the rock mass (Fig. 16), in which the momentum transfer between the rock blocks may cause their fragmentation. What then follows is depicted in the discussion of the DEM model (Sect. 5.1).

Table 4 Further input parameter for DEM

Coefficient of restitution of particle/floor contacts	COR_{floor}	–	0.3	
Friction coefficient of particle/particle contacts	$\mu_{particle}$	–	0.5	Together with an experimentally derived dilation angle of $6°\,\mu_{particle}$ yields an angle of repose of the total assembly of 33° (e.g. [9])
Friction coefficient of particle/ground contacts case I	$\mu_{ground,\,I}$	–	0.5	
Friction coefficient of particle/ground contacts case II	$\mu_{ground,\,II}$	–	9.5	

This would mean that "soft" ground will mobilize a higher resistance than "hard" rock above a critical relative displacement rate between sturzstrom and ground, due to momentum transfer. Such behaviour reverses when the sturzstrom eventually slows down. Without significant momentum transfer, undrained ground will mobilize much lower shear strength than a hard rock surface. The concept of inertial entrainment friction therefore suggests an explanation for the presence of fragmentation during run out of a sturzstrom on soft ground but also of the occurrence of secondary features like, for example, transversal ridges or toma hills (among others e.g. [58,105,106]). Such features seem to be related to situations where sturzstroms have been emplaced on very soft, saturated soils. The sturzstrom may already have come to rest (no or small displacement relative to the direct ground) whereas slabs of failed soil, accelerated due to the momentum transfer described above, may still move, deforming the sturzstrom deposit above. If the heavily fragmented rock mass of a sturzstrom reaches an open water surface, a suspension flow may evolve adding to an even more prolonged total run out. The late deposition phases of the Almtal sturzstrom in Austria [107] or again Goldau in 1806, when the rock mass reached Lake Lauerz [10], may serve as examples. But these suspension flows can not be considered as sturzstroms anymore in the strict sense.

The other extreme are rock blocks sliding on "hard" intact rock. In this case, momentum transfer into the base may be minor because, even at high velocities, substantial ploughing may not occur, preventing migration of the shear zone into the rock mass. This would cause all shearing to take place within this contact zone creating enormous frictional heat, occasionally leading to partial melting of the surrounding rock (e.g. [63]). In any case, the rock mass would move in *this* situation as a block or flexible sheet, displaying small amounts of fragmentation only.

A further inference, which may be drawn from the concept of inertial entrainment friction, is that, if for any reason, the shear resistance between the sturzstrom rock mass and the underground is significantly reduced (for example interstitial volatiles like air, water, fused rock, etc), the rock mass will move as a block or flexible sheet with all displacement taking place in that distinct shear zone. In this case, only minor fragmentation will occur because the relative velocities between
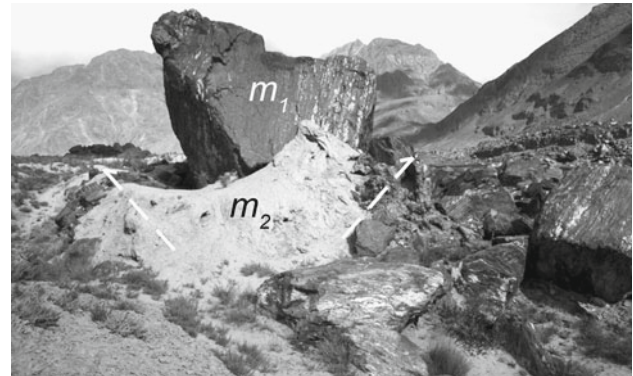

Fig. 17 An example of how rugged terrain may be envisioned in the context with flat, soft ground. The image shows a sturzstrom rock block which ploughed through fine-grained fluvial and lacustrine sediments near the distal rim of the Yarrbah Tshoh event, Shigar valley Baltistan [104]. The sturzstrom moved diagonally from the left to the right. Hewitt [104] notes the "bow-wave" of crumpled alluvium in front of the largest boulder. This means that not only the internal frictional resistance of the alluvium had to be overcome (*arrows*) but also the momentum of the boulder with mass m_1 had to be transferred into the wedge of soil with mass m_2

the particles within the rock mass are too small to generate sufficient impact forces. Because intense fragmentation is characteristic of sturzstroms, any process which may be proposed as reason for a significant reduction of the basal shear resistance (below the angle of repose of the sturzstrom rock mass) may be ruled out from playing a major role in the displacement of sturzstroms. This inference may also allow a new view on the extremely large sturzstroms on the surface of the planet Mars. Their formation, and whether these sturzstroms were emplaced wet or dry, is still in discussion [108–111]. This question has profound implications regarding the presence, extent and timing of ground ice reservoirs and liquid water on Mars.

For now, only a high "apparent friction" is introduced into the DEM to demonstrate the effects of dynamic fragmentation and the applicability of the comminution model after [77]. But the concept of inertial entrainment friction will be explored in more detail in future.

Finally, it is necessary to review the centrifuge experiments again. In Sect. 2.3 it is reported that the rock masses within that experiment moved as a flexible sheet (Fig. 7) *and* displayed a mode of fragmentation, which is compa-

rable to deposits of natural sturzstroms (Fig. 8). From the DEM simulation, it is inferred that both at once may not be possible. At the time, when the centrifuge experiment was designed, it seemed essential to provide a modelling environment in which ploughing and therefore momentum transfer between the rock mass and the side walls of the experimental chute is prevented. The centrifugal experiment replicates therefore the "hard" ground case as discussed above. The observed fragmentation is interpreted to be the result of the dynamic acceleration field evolving from the boundary conditions as discussed in Sects. 2.2.1 and 2.3, acting as a "soft" obstacle. Based on the evidence derived from the DEM, it seems promising to introduce truly "rugged" boundary conditions in the centrifuge in upcoming studies. This may allow momentum transfer, fragmentation and migration of the process zone to be simulated physically at laboratory scale.

6 Conclusion

The evidence presented in this study suggests that the comminution model after [77,85] constitutes a useful tool for the field of sturzstrom research. It allows field evidence and results of physical experiments presented within this study to be linked with numerical modelling, by providing a reasonable mathematical description of fragmentation. At the same time, this comminution model is simple enough to represent key features of fragmentation and make progress in sturzstrom research, while not getting lost in mechanical or mathematical details.

The conclusion is drawn that sturzstroms represent a type of landslide whose run out is not only controlled by friction but significantly by the initial size, intact strength and intact elastic properties of the rocks involved. This allows a number of interesting implications to be suggested on which further research may be based: (1) The empirical volume dependency of the run out of sturzstroms has one physical reason in the amount and initial size of intact rock blocks available for fragmentation and therefore of dispersive stress generation. The volume of intact rock particles involved in such a flow can be envisioned as a "fuel" source consumed by fragmentation. (2) Sturzstroms will develop in situations where the majority of the host rock is constituted of hard, widely jointed blocks (e.g. [112]). Otherwise the development of slow, deep seated gravitational slides, is more likely [113]. The investigation of the structural inventory of the detachment zone of a sturzstrom therefore gains significance (for a study covering this topic e.g. [97]). (3) The sturzstrom model discussed here depends on the presence of "rugged" ground to allow for fragmentation of the rock mass and a migration of the shear zone into the sturzstrom. (4) The mathematical descriptions of

comminution, and the resulting development of dispersive stresses presented here are suitable to be implemented as constitutive models within distinct element codes. A calculation-efficient numerical simulation of the effects of fragmentation within a particulate flow, under consideration of all effects of three-dimensional momentum transfer, may now possible.

The centrifuge experiments allow these mathematical algorithms implemented within the distinct element model to simulate the effects of dynamic fragmentation, to be causatively tracked all the way through their analytical description, to the empirical evidence gained from the observation of true sturzstroms.

Finally the implications presented in the discussion may suggest that a sturzstrom, because of its strong relation to internal fragmentation, constitutes a landslide category of its own. This proposition does not exclude the possible appearance of frictionites, toma hills or suspension flows etc., but it considers them as secondary features.

References

1. Cruden, D.M., Varnes, D.J.: Landslide types and processes. In: Turner, A.K., Schuster, R.L. (eds.) Landslides—Investigation and Mitigation, Special Report 247, pp. 36–75. Transportation Research Board, National Research Council, National Academy Press, Washington DC (1996)
2. Carson, M.A., Kirkby, M.J.: Hillslope Form and Process. Cambridge University Press, Cambridge (1972)
3. Scheidegger, A.E.: Theoretical Geomorphology. Springer, Berlin, Heidelberg, Germany (1991)
4. Duncan, J.M.: Soil slope stability analysis. In: Turner, A.K., Schuster, R.L. (eds.) Landslide—Investigation and Mitigation, pp. 337–371. Transportation Research Board, National Research Council, Washington, DC (1996)
5. Norrish, N.I., Wyllie, D.C.: Rock slope stability analysis. In: Turner, A.K., Schuster, R.L. (eds.) Landslides—Investigation and Mitigation, pp. 391–428. Transportation Research Board, National Research Council, Washington, DC (1996)
6. Hsü, K.J., Albert, Heim : Observations on landslides and relevance to modern interpretations. In: Voight, B. (ed.) Rockslides and Avalanches, pp. 71–93. Elsevier, Amsterdam The Netherlands (1978)
7. Hsü, K.J.: Catastrophic debris streams (sturzstroms) generated by rockfalls. Geol. Soc. Am. Bull. **86**(50117), 129–140 (1975)
8. Collins, G.S., Melosh, H.J.: Acoustic fluidisation and the extraordinary mobility of sturzstroms. J. Geophsy. Res. **108**(B10), 2473 (2003)

9. Eisbacher, G.H., Clague, J.J.: Destructive mass movements in high mountains: Hazard and management. Geological Survey of Canada (1984)

10. Heim, A.: Bergsturz und Menschenleben. Naturforschende Gesellschaft in Zürich, Zürich, Switzerland (1932)

11. Itasca: Theory and background. In: PFC-3D Version 3.1, pp. 2.19–12.22. Itasca Consulting Group, Inc., Minneapolis, Minnesota (2005)

12. Cundall, P.A.: Formulation of a three-dimensional distinct element model–part i. A scheme to detect and represent contacts in a system composed of many polyhedral blocks. Int. J. Rock Mech. Min. Sci. Geomech. Abs. 25(3), 107–116 (1988)

13. Cundall, P.A., Strack, O.D.L.: A discrete numerical model for granular assemblies. Geotechnique 29(1), 47–65 (1979)

14. Hart, R., Cundall, P.A., Lemos, J.: Formulation of a three-dimensional distinct element model–part ii. Mechanical calculations for motion and interaction of a system composed of many polyhedral blocks. Int. J. Rock Mech. Min. Sci. Geomech. Abs. 25(3), 117–125 (1988)

15. Springman, S., Laue, J., Boyle, R., White, J., Zweidler, A.: The ETH Zurich geotechnical drum centrifuge. Int. J. Phys. Model. Geotech. 1(1), 59–70 (2001)

16. Lauth, B., Sareiter, J.: Wissenschaftliche Erkenntnis. Mentis Verlag, Paderborn, Germany (2005)

17. Rosenberg, A.: Philosophy of Science. Routledge, New York (2005)

18. Oreskes, N., Shrader-Frechette, K., Belitz, K.: Verification, validation, and confirmation of numerical models in the earth sciences. Science 263, 641–646 (1994)

19. Mayne, P.W., Coop, M.R., Springman, S.M., Huang, A.-B., Zornberg, J.G.: Geomaterial behavior and testing—Comportement et essai de Geomaterial, 17th International Conference on Soil Mechanics & Geotechnical Engineering, ICSMGE, pp. 2777-2872, Alexandria, Egypt, 5–9 October, 2009

20. Lee, F.H.: The philosophy of modelling versus testing. In: Springman, S. (ed.) Constitutive and Centrifuge Modelling: Two Extremes, pp. 113–131. Balkema, Centro Stefano Franscini, Monte Verità, Asona, Switzerland (2002)

21. Strom, A.L.: Morphology and internal structure of rockslides and rock avalanches: Grounds and constraints for their modelling. In: Evans, S.G., Mugnozza, G.S., Strom, A., Hermanns, R.L. (eds.) Landslides from Massive Rock Slope Failure, pp. 305–326. Springer, The Netherlands (2006)

22. Scheidegger, A.E.: On the prediction of the reach and velocity of catastrophic landslides. Rock Mech. 5, 231–236 (1973)

23. Davies, T.R.H.: Spreading of rock avalanche debris by mechanical fluidization. Rock Mech. 15, 9–24 (1982)

24. Legros, F.: The mobility of long-runout landslides. Eng. Geol. 63(3–4), 301–331 (2002)

25. Davies, T.R.H., McSaveney, M.J.: Runout of dry granular avalanches. Can. Geotech. J. 36, 313–320 (1999)

26. Di Luzio, E., Bianchi-Fasani, G., Esposito, C., Saroli, M., Cavinato, G.P., Scarascia-Mugnozza, G.: Massive rock slope failure in the central Apennines (Italy): The case of the Campo di Giove rock avalanche. Bull. Eng. Geol. Environ. 63, 1–12 (2004)

27. Strom, A.L.: Mechanisms of stratification and abnormal crushing of rockslide deposits. In: Oliveira, R. (ed.) 7th International Association for Engineering Geology and the Environment (IAEG) Congress, pp. 1287–1295. Balkema, Lisbon, Portugal (1994)

28. Strom, A.L.: Some morphological types of long-runout rockslides: Effect of the relief on their mechanism and on the rockslide deposits distribution. In: Senneset, K. (ed.) 7th International Symposium on Landslides, pp. 1977–1982. Balkema, Trondheim (1996)

29. Friedmann, S.J., Taberlet, N., Losert, W.: Rock-avalanche dynamics: Insights from granular physics experiments. Int. J. Earth Sci. 95(5), 911–919 (2006)

30. Smith, G.M., Davies, T.R., McSaveney, M.J., Bell, D.H.: The Acheron rock avalanche, Canterbury, New Zealand—morphology and dynamics. Landslides 3, 62–72 (2006)

31. Pollet, N., Schneider, J.-L.M.: Dynamic disintegration processes accompanying transport of the Holocene Flims sturzstrom (Swiss Alps). Earth Planet. Sci. Lett. 221(1–4), 433–448 (2004)

32. Schneider, J.-L.M., Wassmer, P., Ledésert, B.: The fabric of the sturzstrom of Flims (Swiss Alps): Characteristics and implications on the transport mechanisms. C. R. Acad. Sci. Ser. IIA. Earth Planet. Sci. 328(9), 607–613 (1999)

33. Couture, R., Locat, J., Drapeau, J.-P., Evans, S.G., Hadjigeorgiou, J.: Evaluation de la granulométrie à la surface des débris d'avalanche rocheuse. In: Moore D., Hungr O. (eds.) 8th International Congress International Association for Engineering Geology and the Environment, pp.1383–1390. Balkema, Vancouver, Canada (1998)

34. Shoaei, Z., Ghayoumian, J.: Seimareh landslide, the largest complex slide in the world. In: Moore, D., Hungr, O. (eds.) 8th International Congress International Association for Engineering Geology and the Environment, pp. 1337–1342. Balkema, Vancouver, Canada (1998)

35. Eppler, D.B., Fink, J., Fletcher, R.: Rheologic properties and kinematics of emplacement of the Chaos Jumbles rockfall avalanche, Lassen Volcanic national park, California. J. Geophsy. Res. 92(B5), 3623–3633 (1987)

36. Erismann T.H. Abele G.: Dynamics of Rockslides and Rockfalls. Springer, Berlin, Heidelberg, Germany (2001)

37. Harp, E.L., Jibson, R.W., Kayen, R.E., Keefer, D.K., Sherrod, B.L., Carver, G.A., Collins, B.D., Moss, R.E.S., Sitar, N.: Landslides and liquefaction triggered by the m 7.9 Denali fault earthquake of 3 November 2002. GSA Today 13(8), 4–10 (2003)

38. McSaveney, M.J.: Sherman glacier rock avalanche, Alaska, U.S.A. In: Voight, B (ed.) Rockslides and Avalanches, 1, Natural Phenomena, pp. 439–479. Elsevier, The Netherlands (1978)

39. Legros, F.: Landslide mobility and the role of water. In: Evans, S.G., Mugnozza, G.S., Strom, A., Hermanns, R.L. (eds.) Landslides from Massive Rock Slope Failure, pp. 233–242. Springer, The Netherlands (2006)

40. Shaller, P.J., Smith-Shaller, A.: Review of proposed mechanisms for sturzstroms (long-runout landslides). In: Abbott, P.L., Seymour, D.C. (eds.) Sturzstroms and Detachment Faults, Anza-Borrego Desert State Park, California, pp. 185–202. South Coast Geol. Soc. Inc., Santa Ana, CA (1996)

41. Deganutti, A.M.: The hypermobility of rock avalanches. Ph.D.-Thesis, Università Degli Studi di Padova, Padova/Italy (2008)

42. Pirulli, M., Scavia, C.: An overview of numerical models for rock avalanche runout analysis. In: Ribeiro e Sousa, L., Olalla, C., Grossmann, N. (eds.) 11th Congress of the International Society for Rock Mechanics (ISRM), pp. on CD. Taylor & Francis Group, Lisbon (2007)

43. Campbell, C.S., Cleary, P.W., Hopkins, M.: Large-scale landslide simulations: Global deformation, velocities and basal friction. J. Geophsy. Res. 100(B5), 8267–8283 (1995)

44. Bagnold, R.A.: Experiments on a gravity-free dispersion of large solid spheres in a Newtonian fluid under shear. Proc. Royal Soc. London 255, 49–63 (1954)

45. Campbell, C.S.: Self-lubrication for long runout landslides. J. Geol. 97(6), 653–665 (1989)

46. Davies, T.R.H, McSaveney, M.J., Hodgson, K.A.: A fragmentation-spreading model for long-runout rock avalanches. Canad. Geotech. J. 36, 1096–1110 (1999)

47. McSaveney, M.J., Davies, T.R.H.: Rapid rock-mass flow with dynamic fragmentation: Inferences from the morphology, and

internal structures of rockslides and avalanches. In: Evans, S.G., Martino, S. (eds.) Massive Rock Slope Failure: New Models for Hazard Assessment, pp. 89–92. NATO Advanced Research Workshop, Celano (AQ), Abruzzo, Italy (2002)

48. Davies, T.R.H., McSaveney, M.J.: The role of rock fragmentation in the motion of large landslides. Eng. Geol. **109**(1–2), 67–79 (2009)

49. Davies, T.R.H., McSaveney, M.J., Deganutti, A.M.: Dynamic fragmentation causes low rock-on-rock friction. In: 1st Canada-U.S. Rock Mechanics Symposium, Vancouver, Canada (2007)

50. McSaveney, M.J., Davies, T.R.H.: Surface energy is not one of the energy losses in rock comminution. Eng. Geol. **109**(1–2), 109–113 (2009)

51. Berner C.: (2004) Der Bergsturz von Goldau. MSc Thesis, ETH Zürich, Zurich, Switzerland

52. Zehnder, J.N.: Der Goldauer Bergsturz. Verlag Stiftung Bergsturzmuseum Goldau, Goldau, Switzerland (1988)

53. Buxtorf, A., Baumberger, E., Niethammer, G., Arbenz, P.: Erläuterungen zur geologischen Karte der Rigihochfluhkette. In: Geologische Karte der Schweiz: Geologische Kommission der Schweizer. Naturforschenden Gesellschaft (1916)

54. Erismann, T.H.: Mechanisms of large landslides. Rock Mech. **12**, 15–46 (1979)

55. Zay, K.: Goldau und seine Gegend: Wie sie war und was sie geworden. Orell, Füssli und Compagnie, Zurich/Switzerland (1807)

56. Thuro, K., Berner, C., Eberhardt, E.: Der Bergsturz von Goldau 1806—200 Jahre nach dem Ereignis. Felsbau **24**(3), 59–66 (2006)

57. Poschinger, A.v: The Flims rockslide; new aspects of its mechanism and impact. In: Evans, S.G., Martino, S. (eds.) Massive Rock Slope Failure: New Models for Hazard Assessment, pp. 114–116. NATO Advanced Research Workshop, Celano (AQ), Abruzzo, Italy (2002)

58. Poschinger, A.v., Wassmer, P., Maisch, M.: The Flims rockslide: History of interpretation and new insights. In: Evans, S.G., Mugnozza, G.S., Strom, A., Hermanns, R.L. (eds.) Landslides from Massive Rock Slope Failure, pp. 329–356. Springer, The Netherlands (2006)

59. Wassmer, P., Schneider, J.L., Poller, N.: The "playing cards" model as a tool to better understanding long run-out: The case of the Flims Holocene sturzstrom. In: Evans, S.G., Martino, S. (eds.) Massive Rock Slope Failure: New Models for Hazard Assessment, pp. 152–155. NATO Advanced Research Workshop, Celano (AQ), Abruzzo, Italy (2002)

60. Wassmer, P., Schneider, J.L., Pollet, N., Schmitter-Voirin, C.: Effects of the internal structure of a rock–avalanche dam on the drainage mechanism of its impoundment, Flims sturzstrom and Ilanz paleo-lake, Swiss Alps. In Geomorphology, pp. 3–17: Elsevier (2004)

61. Montandon, F.: Chronologie des grands éboulements alpins, du début de l'ère chrétienne a nos jours. Matériaux Pour l'étude Des calamités, Société de Géographie, Genève **32**, 271–340 (1933)

62. Brückl, E., Brückl, J., Heuberger, H.: Present structure and prefailure topography of the giant rockslide of Köfels. Z. Gletscherkunde Glaziogeologie **37**(1), 49–79 (2001)

63. Erismann, T., Heuberger, H., Preuss, E.: Der Bimsstein von Köfels (Tirol), ein Bergsturz-"Friktionit". Mineral. Petrol. **24**(1), 67–119 (1977)

64. Stini, J.: Unsere Täler wachsen zu. Geologie Bauwes. **13**, 71–79 (1941)

65. Ashby, M.F., Jones, D.R.H.: Engineering Materials. Pergamon Press, Oxford, England (1980)

66. Harder, N.A.: Brittleness, fracture energy and size effect in theory and reality. Mater. Struct. **25**, 102–106 (1992)

67. Engelder, T., Fischer, M.P.: Loading configurations and driving mechanisms for joints based on the Griffith energy-balance concept. Tectonophysics **256**(1–4), 253–277 (1996)

68. van Vliet, M.R.A., van Mier, J.G.M.: Experimental investigation of size effect in concrete and sandstone under uniaxial tension. Eng. Fract. Mech. **65**, 165–188 (2000)

69. van Mier, J.G.M., van Vliet, M.R.A.: Uniaxial tension test for the determination of fracture parameters of concrete: State of the art. Eng. Fract. Mech. **69**, 235–247 (2002)

70. Hillerborg, A.: Results of three comparative test series for determining the fracture energy GF of concrete. Mater. Struct. **18**(5), 407–413 (1985)

71. Schubert, H.: Aufbereitung Fester Mineralischer Rohstoffe. VEB Deutscher Verlag für Grundstoffindustrie, Leipzig, Germany (1989)

72. Imre, B., Wildhaber, B., Springman, S.M.: A physical analogue material to simulate sturzstroms. Eng. Geol. In revision (2009)

73. Räbsamen, S.: Die Energiebilanz von Rutschungen aus trockenem, nicht fragmentierendem Reibungsmaterial in der geotechnischen Trommelzentrifuge am Institut für Geotechnik an der ETH in Zürich. MSc Thesis, ETH, Zurich, Switzerland (2007)

74. McDowell, G.R.: Statistics of soil particle strength. Géotechnique **51**(10), 897–900 (2001)

75. McDowell, G.R., Bolton, M.D.: On the micromechanics of crushable aggregates. Géotechnique **48**(5), 667–679 (1998)

76. McDowell, G.R., Harireche, O.: Discrete element modelling of soil particle fracture. Géotechnique **52**(2), 131–135 (2002)

77. Sammis, C., King, G., Biegel, R.: The kinematics of gouge deformation. Pure Appl. Geophys. **125**(5), 777–812 (1987)

78. McDowell, G.R., Daniell, C.M.: Fractal compression of soil. Géotechnique **51**(2), 173–176 (2001)

79. Einav, I.: Breakage mechanics—part i: Theory. J. Mech. Phys. Solids **55**(6), 1274–1297 (2007)

80. Mandelbrot, B.B.: The Fractal Geometry of Nature. W.H. Freeman, San Francisco/CA (1982)

81. Turcotte, D.L.: Fractals and fragmentation. J. Geophs. Res. **91**(B2), 1921–1926 (1986)

82. Tyler, S.W., Wheatcraft, S.W.: Fractal scaling of soil particle-size distributions: Analysis and limitations. Soil Sci. Soc. Am. J. **56**(2), 362–369 (1992)

83. Diaz-Zorita, M., Grove, J.H., Perfect, E.: Sieving duration and sieve loading impacts on dry soil fragment size distributions. Soil Tillage Res. **94**, 15–20 (2007)

84. Crosta, G.B., Frattini, P., Fusi, N.: Fragmentation in the Val Pola rock avalanche, Italian Alps. J. Geophsy. Res. **112**(F01006), 1–23 (2007)

85. Steacy, S.J., Sammis, C.G.: An automaton for fractal patterns of fragmentation. Nature **353**(6341), 250–252 (1991)

86. McSaveney, M., Davies, T.R.H.: Rockslides and their motion. In: Sassa, K., Fukuoka, H., Wang, F., Wang, G. (eds.) Progress in Landslide Science, pp. 113–133. Springer, Berlin Heidelberg (2007)

87. Davies, T.R.H., McSaveney, M.J.: Inferences from the morphology and internal structure of rockslides and rock avalanches rapid rock mass flow with dynamic fragmentation. In: Evans, S.G., Mugnozza, G.S., Strom, A., Hermanns, R.L. (eds.) Landslides from Massive Rock Slope Failure, pp. 285–304. Springer, The Netherlands (2006)

88. Grady, D.E., Kipp, M.E.: Dynamic rock fragmentation. In: Atkinson, B.K. (ed.) Fracture Mechanics of Rock, pp. 429–475. Academic Press, London (1987)

89. Herget, G.: Stresses in Rock. Balkema, Rotterdam, The Netherlands (1988)

90. Vardoulakis, I.: Rock bursting as a surface instability phenomenon. Int. J. Rock Mech. Mining Sci. Geomech. Abs. **21**(3), 137–144 (1984)

91. Terzaghi, K.: From Theory to Practice in Soil Mechanics. Wiley, New York (1960)

92. Jaeger, J.C., Cook, N.G.W.: Fundamentals of Rock Mechanics. Chapman and Hall, Great Britain (1979)

93. Imre, B., Räbsamen, S., Springman, S.M.: A coefficient of restitution of rock materials. Comp. Geosci. **34**, 339–350 (2008)

94. Howe, S., Goldsmith, W., Sackman, J.: Macroscopic static and dynamic mechanical properties of yule marble. Exp. Mech. **14**(9), 337–346 (1974)

95. Zhao, J.: Applicability of Mohr–Coulomb and Hoek–Brown strength criteria to the dynamic strength of brittle rock. Int. J. Rock Mech. Mining Sci. **37**(7), 1115–1121 (2000)

96. Li, X.B., Lok, T.S., Zhao, J.: Dynamic characteristics of granite subjected to intermediate loading rate. Rock Mech. **38**(1), 21–39 (2005)

97. Locat, P., Couture, R., Leroueil, S., Locat, J., Jaboyedoff, M.: Fragmentation energy in rock avalanches. Canad. Geotech. J. **43**(8), 830–851 (2006)

98. van Vliet, M.R.A.: Size effect in tensile fracture of concrete and rock. PhD Thesis, Technical University Delft, Delft, The Netherlands (2000)

99. Turcotte, D.L.: Fractals and Chaos in Geology and Geophysics. Cambridge University Press, Cambridge, UK (1997)

100. Pollack, H.N.: Uncertain Science...Uncertain World. Cambridge University Press, Cambridge, UK (2003)

101. Imre, B.: The particle flow code, PFC-2D, applied in planetary studies to model the tectonic evolution of chasma walls on Mars. In: Shimizu, Y., Hart, R.D., Cundall, P.A. (eds.) 2nd International PFC Symposium: Numerical Modeling in Micromechanics via Particle Methods, pp. 199-206. Balkema, Kyoto, Japan (2004)

102. Potyondy, D.O., Cundall, P.A.: A bonded-particle model for rock. Int. J. Rock Mech. Mining Sci. **41**(8), 1329–1364 (2004)

103. Atkinson, J.H., Bransby, P.L.: The Mechanics of Soils : An Introduction to Critical State Soil Mechanics. McGraw-Hill, London [etc.] (1978)

104. Hewitt, K.: Rock avalanches with complex run out and emplacement, Karakoram Himalaya, Inner Asia. In: Evans, S.G., Mugnozza, G.S., Strom, A., Hermanns, R.L. (eds.) Landslides from Massive Rock Slope Failure, pp. 521–550. Springer, The Netherlands (2006)

105. Abele, G.: Bergstürze in den Alpen. Deutscher und Österreichischer Alpenverein, München (1974)

106. Prager, C., Krainer, K., Seidl, V., Chwatal, W.: Spatial features of holocene sturzstrom-deposits inferred from subsurface investigations (Fernpass rockslide, Tyrol, Austria). Geo. Alp **3**, 147–166 (2006)

107. Reitner, J., Lang, M., van Husen, D.: Deformation of high slopes in different rocks after Würmian deglaciation in the Gailtal (Austria). Quater. Int. **18**, 43–51 (1993)

108. Lucchitta, B.K., McEwen, A.S., Clow, G.D., Geissler, P.E., Singer, R.B., Schultz, R.A., Squyres, S.W.: The canyon system on Mars. In: Kieffer, H.H., Jakosky, B.M., Snyder, C.W., Matthews, M.S. (eds.) Mars, pp. 453–492. University of Arizona Press, Tucson & London (1992)

109. Caruso, P.A., Schultz, R.A.: Slope stability and lithology for interior layered deposits and wallrock in Valles Marineris. Lunar Planet. Sci. **32**, 1745 (2001)

110. Schultz, R.A.: Stability of rock slopes in Valles Marineris, Mars. Geophys. Res. Lett. 29, 19, 1932, 38-31—38-34 (2002)

111. Melosh, H.J.: Giant rock avalanches. Nature **3348**, 483–484 (1990)

112. ISRM: International society for rock mechanics commission on standardization of laboratory and field tests: Suggested methods for the quantitative description of discontinuities in rock masses. Int. J. Rock Mech. Mining Sci. Geomech. Abs. 15, 6, 319-368 (1978)

113. Imre, B., Alig, C., Schönenberger, I., Springman, S.M., Hermann, S.: Morphology and kinematic of a very large, deep-seated structural rock slide located in the Fusch valley, Eastern Alps, Austria. Geomorphology **112**(3–4), 277–294 (2009)

114. Voight, B., Pariseau, W.G.: Rockslides and avalanches: An introduction. In: Voight, B. (ed.) Rockslides and Avalanches, 1, Natural Phenomena, pp. 1–63. Elsevier, The Netherlands (1978)

115. Shreve, R.L.: Sherman landslide, Alaska. Science **154**(3757), 1639–1643 (1966)